*Article*

# A Power Supply System with ZVS and Current-Doubler Features for Hybrid Renewable Energy Conversion

**Cheng-Tao Tsai [1], Chih-Lung Shen [2],* and Jye-Chau Su [3]**

[1] Department of Electrical Engineering, National Chin-Yi University of Technology, Taichung 41170, Taiwan; E-Mail: cttsai@ncut.edu.tw

[2] Department of Electronic Engineering, National Kaohsiung First University of Science and Technology, 1 University Rd., Yanchao, Kaohsiung 824, Taiwan

[3] Department of Electronic Engineering, National Chin-Yi University of Technology, Taichung 41170, Taiwan; E-Mail: jc07@ms34.hinet.net

* Author to whom correspondence should be addressed; E-Mail: clshen@ccms.nkfust.edu.tw; Tel.: +886-7-6011000 (ext. 2515); Fax: +886-7-6011386.

**Abstract:** In this paper, a power supply system for hybrid renewable energy conversion is proposed, which can process PV (photovoltaic) power and wind-turbine energy simultaneously for step-down voltage and high current applications. It is a dual-input converter and mainly contains a PV energy source, a wind turbine energy source, a zero-voltage-switching (ZVS) forward converter, and a current-doubler rectifier. The proposed power supply system has the following advantages: (1) PV-arrays and wind-energy sources can alternatively deliver power to the load during climate or season alteration; (2) maximum power point tracking (MPPT) can be accomplished for both different kinds of renewable-energy sources; (3) ZVS and synchronous rectification techniques for the active switches of the forward converter are embedded so as to reduce switching and conducting losses; and (4) electricity isolation is naturally obtained. To achieve an optimally dynamic response and to increase control flexibility, a digital signal processor (DSP) is investigated and presented to implement MPPT algorithm and power regulating scheme. Finally, a 240 W prototype power supply system with ZVS and current-doubler features to deal with PV power and wind energy is built and implemented. Experimental results are presented to verify the performance and the feasibility of the proposed power supply system.

## 1. Introduction

Serious greenhouse effects and limited fossil energy supplies have forced most engineers to do research on renewable energy sources [1]. The typical renewable energy sources include solar, wind and geothermal energies, which have the features of cleanliness, abundance and freedom from maintenance [2]. Currently, solar and wind are most widely utilized renewable energies. Photovoltaic (PV) arrays and wind turbine technologies have been undergoing a dramatic development and now are the world's fastest growing energies. Therefore, to develop PV and wind energy sources to substitute for fossil fuels has been an important topic [3–5].

In general, PV arrays and wind energy are complementary since sunny days in summer are usually calm and strong winds often occur in winter. The curves of their power alterations are shown in Figure 1. Hence, a dual-input PV-wind power supply has higher reliability to deliver continuous power than individual source [6–8]. Usually, two separated DC/DC converters for the PV arrays and the wind turbine are used in a dual-input PV-wind power supply, as shown in Figure 2, in which component count and cost are increased significantly [9–12]. An effective approach is to adopt a dual-input power supply system by combining these renewable energy sources with a DC/DC converter, which can simplify power supply and reduce cost. In order to reduce switching and conducting losses of active switches and improve efficiency, a DC/DC converter with ZVS and synchronous rectification techniques are usually required.

**Figure 1.** Energy curves of PV power and wind power for season alteration.
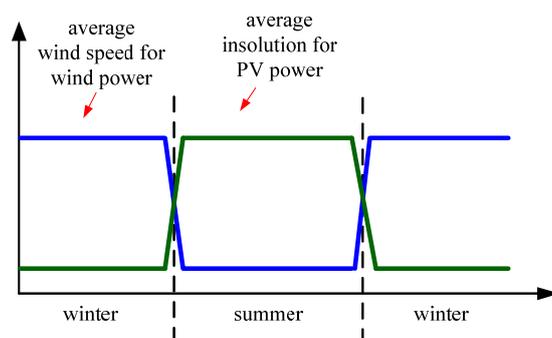


**Figure 2.** Two separated DC/DC converters for PV arrays and wind turbine conversion.
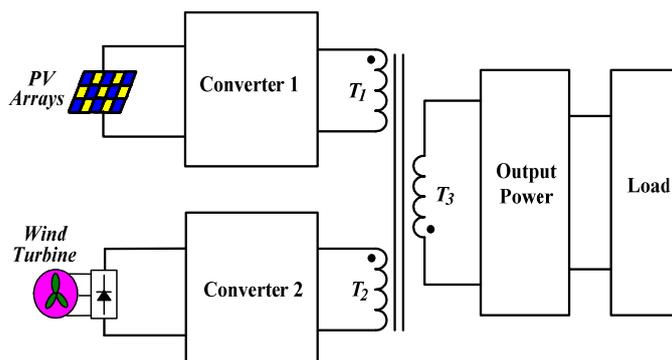
In this paper, a dual-input power supply system with a ZVS forward converter and a current-doubler rectifier for renewable PV arrays and wind energy applications is proposed, as shown in Figure 3. In order to obtain the optimal power conversion from the PV arrays and wind turbine energy, MPPT methods, ZVS and synchronous rectification techniques must be incorporated [13–17]. Thus, the proposed dual-input power supply has the following main features: (1) PV arrays and wind turbine energies can alternatively deliver power to the load during climate or season alteration; (2) a simple perturbation-and-observation method and a DSP microcontroller are incorporated to realize the MPPT algorithm and power regulating scheme; (3) ZVS and synchronous rectification techniques are implemented to reduce switching and conducting losses of active switches; and (4) electricity isolation is naturally obtained by the use of a high-frequency transformer in the soft-switching forward converter.

The structural description of the proposed dual-input power supply system is described in Section 2. The MPPT Algorithm of PV arrays and wind turbine with a simple perturbation-and-observation method is described in Section 3. The control scheme of the proposed power supply system is decribed in Section 4. Design consideration of soft-switching forward converter is decribed in Section 5. Experimental results obtained from a 240 W prototype with the proposed dual-input power supply system for PV arrays and wind turbine energy source are presented in Section 6. Finally, conclusions are given in Section 7.

**Figure 3.** Circuit structure of the proposed power supply system.
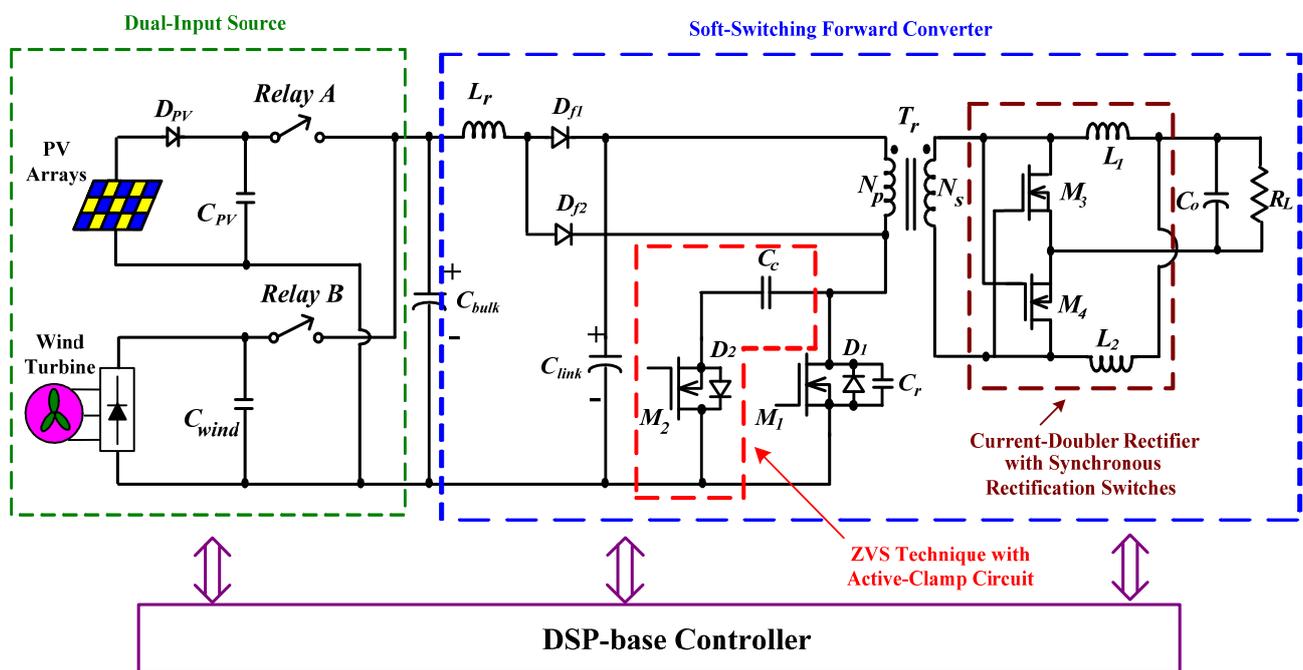


## 2. Structural Description of the Proposed Power Supply System

Figure 3 shows the structure of the proposed power supply system, which is composed of a ZVS forward converter and a current-doubler rectifier with synchronous rectification switches. The ZVS technique and operational principle of the proposed power supply system are described as follows:

## 2.1. Selection of ZVS Circuit

Converters using the ZVS technique will result in no voltage across an active switch to avoid concurrent high voltage during turn-on transition, as illustrated in Figure 4. Thus, a ZVS operation is an effective technique to solve or alleviate switching losses and converter stress problems. ZVS techniques can be roughly classified as passive-clamp and active-clamp circuits [18,19]. Passive-clamp circuits use only passive elements (diodes, capacitors and inductors, *etc.*) to perform ZVS operation. Active-clamp circuits add one or more active switches along with other passive elements to perform ZVS operation. Although the passive-clamp circuits do not require extra active switches or additional control circuits, they usually require more diodes and energy-storage components, which might increase the complexity of any printed circuit board (PCB) layout and induce a high level of EMI noise. In practice, active-clamp circuits will provide a relatively simple solution to reduce converter switching losses [18].

**Figure 4.** Illustration of ZVS for an active switch.
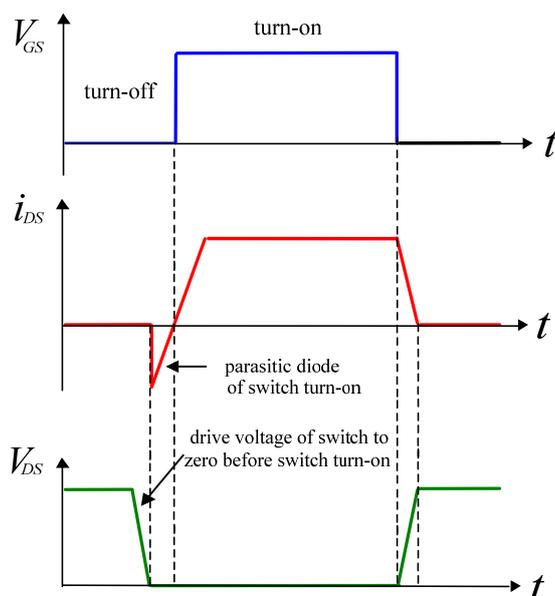


In this study, a dual-input power supply system with a ZVS forward converter for renewable energy applications is proposed, as shown in Figure 3. The ZVS forward converter with an active-clamp circuit can effectively alleviate voltage stresses and reduce switching losses of active switches. In addition, the current-doubler rectifier with synchronous rectification technique can also reduce conducting losses of active switches. Thus, conversion efficiency of a dual-input power supply system can be increased significantly.

## 2.2. Operational Principle

For convenience of illustration and analysis, Figure 3 is simplified and redrawn in Figure 5. The proposed ZVS forward converter consists of resonant inductor $L_r$, main switch $M_1$, resonant capacitor $C_r$, clamp capacitor $C_c$, auxiliary switch $M_2$, transformer $T_r$, synchronous rectification switches $M_3$ and $M_4$, inductors $L_1$ and $L_2$, and output filter capacitor $C_o$. In order to achieve the ZVS feature for main

switch $M_1$ and auxiliary switch $M_2$, the resonant inductor $L_r$ and capacitor $C_r$ are usually required. Additionally, the active switches $M_3$ and $M_4$ are driven with synchronous rectification technique to reduce conduction losses. Therefore, the conversion efficiency of proposed power supply can be increased significantly.

**Figure 5.** Simplified circuit diagram of the proposed power supply system.
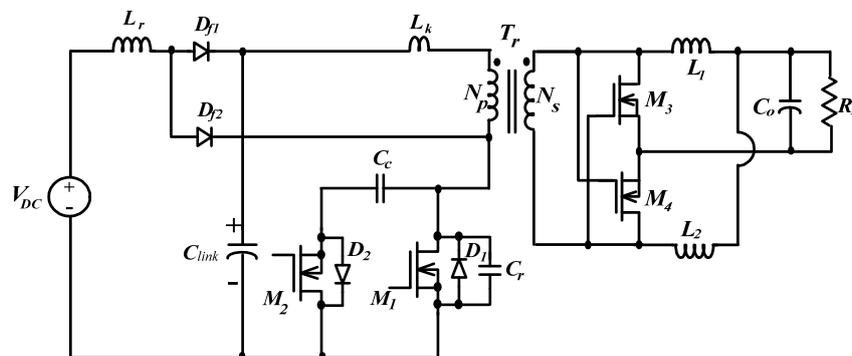


To facilitate the analysis of operation, Figure 6 shows current and voltage waveforms of the key components and the driving signal switches ($M_1$ and $M_2$).

**Figure 6.** Driving signals and key waveforms of the proposed power supply system.
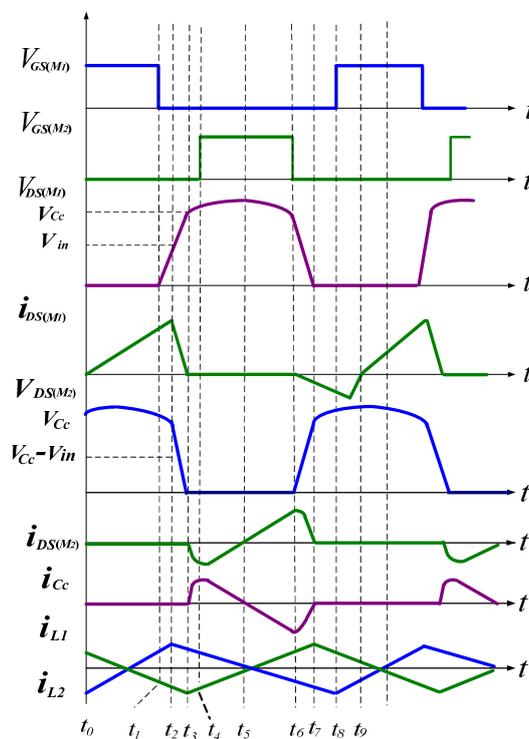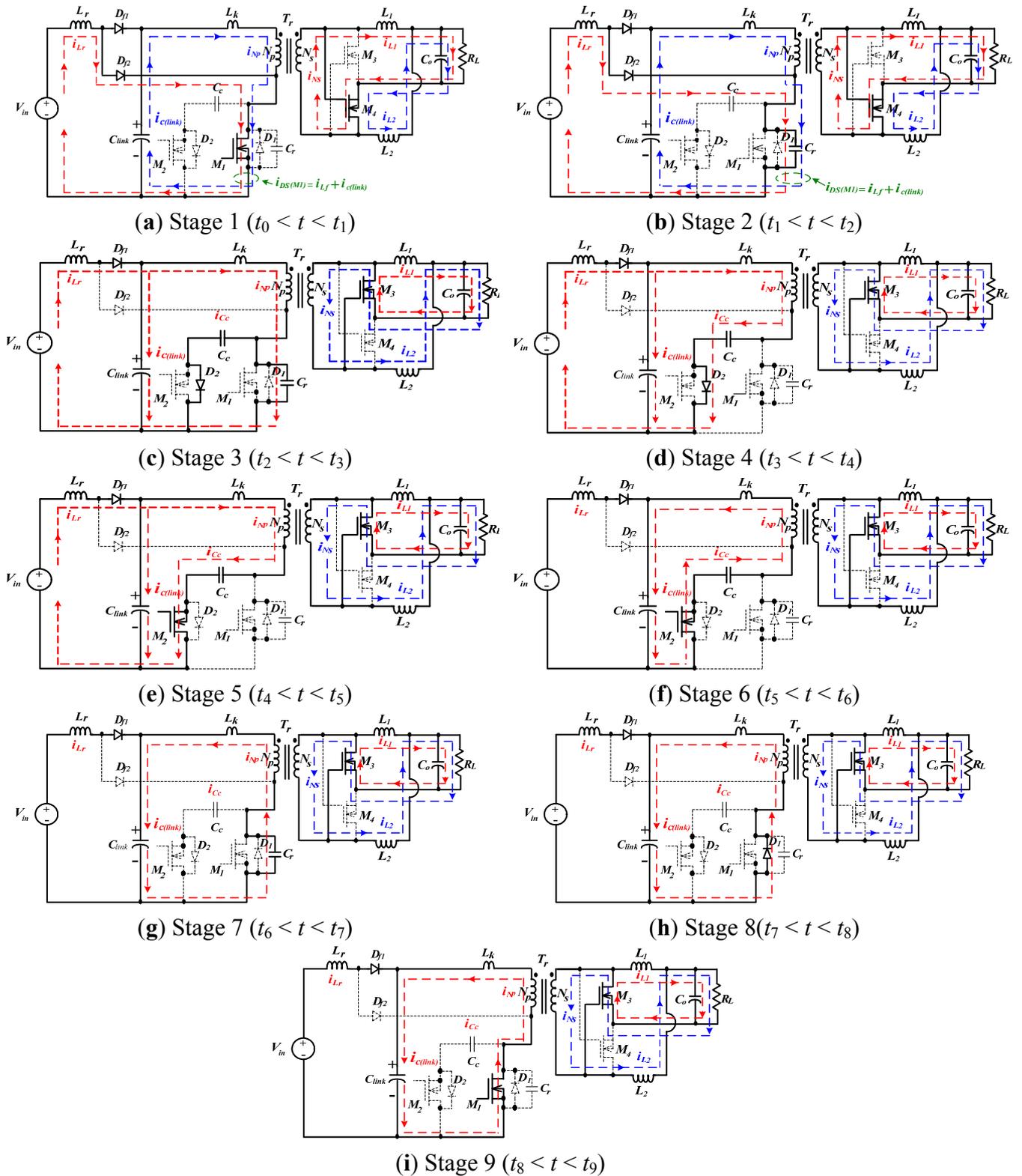


Figure 7 shows the topological stages of the proposed power supply during a switching cycle. To simplify the description of the operational stages, the following assumptions are made.

(1) To analyze the ZVS feature of active switches ($M_1$ and $M_2$), the body diodes ($D_1$ and $D_2$) of the active switches ($M_1$ and $M_2$) and the leakage inductance ($L_k$) of the transformer ($T_r$) will be considered at the steady-state operation of the circuit.

(2) Output capacitor $C_o$ and clamp capacitor $C_c$ are large enough so that the voltages across them are constant over a switching period.

(3) All of the switching devices and components are ideal.

**Figure 7.** Equivalent circuits of operating stages for the proposed power supply system.



(**a**) Stage 1 ($t_0 < t < t_1$)

(**b**) Stage 2 ($t_1 < t < t_2$)

(**c**) Stage 3 ($t_2 < t < t_3$)

(**d**) Stage 4 ($t_3 < t < t_4$)

(**e**) Stage 5 ($t_4 < t < t_5$)

(**f**) Stage 6 ($t_5 < t < t_6$)

(**g**) Stage 7 ($t_6 < t < t_7$)

(**h**) Stage 8($t_7 < t < t_8$)

(**i**) Stage 9 ($t_8 < t < t_9$)

Based on the above assumptions, operation of the proposed converter over one switching cycle can be divided into nine stages. The operational principle is explained stage by stage as follows:

Stage 1 (Figure 7a, $t_0 < t < t_1$)

At time $t_0$, the main switch $M_1$ is turned on, and the resonant inductor current $i_{Lr}$ is flowing through the diode $D_{f2}$ and the switch $M_1$. Simultaneously, the dc-link capacitor $C_{link}$ discharges through the primary winding of the transformer, as shown in Figure 7a. The current $i_{DS(M1)}$ flowing through the switch $M_1$ is the sum of current $i_{Lr}$ and $i_{c(link)}$, which is linearly increased. During this interval, the DC-link capacitor $C_{link}$ energy will be transferred to the secondary through the transformer, and current $i_{NS}$ in the secondary winding of the transformer can be expressed as:

$$i_{NS} = \frac{N_P}{N_S} i_{NP} \tag{1}$$

At this operation, there will be a voltage across the secondary winding, which will turn on the synchronous switch $M_4$ and turn off the synchronous switch $M_3$. The inductor current $i_{L1}$ in the secondary winding will flow through the inductor $L_1$ to the load, and the current $i_{L2}$ of the inductor $L_2$ is in free-wheeling through the switch $M_4$ to the load.

Stage 2 (Figure 7b, $t_1 < t < t_2$)

The main switch $M_1$ is turned off at time $t_1$, and the parasitic capacitor $C_1$ of the switch $M_1$ will be linearly charged by the current $i_{DS(M1)}$ ($= i_{Lr} + i_{c(link)}$). Due to the charge time of the parasitic capacitor $C_1$ is very short, the voltage $V_{DS(M1)}$ of the main switch $M_1$ will be steeply risen. The resonant inductor current $i_{Lr}$ still continuously flows through the switch $M_1$, and its equation can be given as follows:

$$\frac{di_{Lr}}{dt} = \frac{V_{in} - V_{DS(M1)}}{L_r} \tag{2}$$

Stage 3 (Figure 7c, $t_2 < t < t_3$)

At time $t_2$, the voltage $V_{DS(M1)}$ of the main switch $M_1$ is increased over the input voltage $V_{in}$, and the resonant inductor current $i_{Lr}$ begins reduction linearly. Thus, the diode $D_{f2}$ is reversely biased and $D_{f1}$ is forwardly biased. During this interval, the resonant capacitor $C_r$ with the main switch $M_1$ in parallel is maintained charging.

In the secondary winding of the transformer, due to the change of the voltage polarity, the synchronous switch $M_4$ is turned off and $M_3$ is turned on. The current $i_{L2}$ flowing through the inductor $L_2$, output load and synchronous rectifier switch $M_3$ is increased linearly. Simultaneously, the current $i_{L1}$ flowing through the inductor $L_1$, output load and synchronous rectifier switch $M_3$ is decreased linearly. The equivalent circuit is shown in Figure 7c.

Stage 4 (Figure 7d, $t_3 < t < t_4$)

When the voltage $V_{DS(M1)}$ of the main switch $M_1$ is equal to the voltage $V_{Cc}$ of the clamping capacitor, the body diode $D_2$ of the auxiliary switch $M_2$ is conducted and creates a ZVS feature for $M_2$. The resonant inductor current $i_{Lr}$ is diverted to dc-link capacitor $C_{link}$ and clamping capacitor $C_c$. The equivalent circuit is shown in Figure 7d.

Stage 5 (Figure 7e, $t_4 < t < t_5$)

At time $t_4$, the auxiliary switch $M_2$ is turned on under ZVS condition. The resonant inductor current $i_{Lr}$ is diverted to capacitors $C_{link}$ and $C_c$, continuously. During this interval, the secondary current flow is the same as that during $t_3$–$t_4$ interval. The equivalent circuit is shown in Figure 7e.

Stage 6 (Figure 7f, $t_5 < t < t_6$)

When the resonant inductor current $i_{Lr}$ reaches zero at time $t_5$, the operation of circuit enters a discontinuous conduction mode (DCM) and both diodes $D_{f1}$ and $D_{f2}$ are reversely biased. Within this stage, the current is reversed and flowing through clamping capacitor $C_c$ and the transformer to the DC-link capacitor $C_{link}$. The secondary current flow is the same as that during $t_4$–$t_5$ interval. The equivalent circuit is shown in Figure 7f.

Stage 7 (Figure 7g, $t_6 < t < t_7$)

At time $t_6$, the auxiliary switch $M_2$ is turned off. The reverse current will continue to flow through the DC-link capacitor and the resonant capacitor $C_r$. The voltage $V_{DS(M1)}$ of the main power switch $M_1$ will be decreased in the resonant manner towards zero. During this stage, the secondary current flow is the same as that during $t_5$–$t_6$ interval. The equivalent circuit is shown in Figure 7g.

Stage 8 (Figure 7h, $t_7 < t < t_8$)

When the voltage $V_{DS(M1)}$ across $M_1$ has been decreased to zero at time $t_7$, the body diode $D_1$ is conducted to create a ZVS operating feature for $M_1$. The equivalent circuit is shown in Figure 7h.

Stage 9 (Figure 7i, $t_8 < t < t_9$)

The main switch $M_1$ is turned on under ZVS condition at time $t_8$. When the current $i_{DS(M1)}$ is forwardly increased at end of stage 9, the converter operation over one switching cycle is completed. The equivalent circuit is shown in Figure 7i.

## 3. MPPT Algorithm of PV Arrays and Wind Turbine

The typical V-I and output power characteristic curves of the PV arrays with different insolations are shown in Figure 8.

**Figure 8.** Output power and output voltage curves of PV arrays with different insolations.
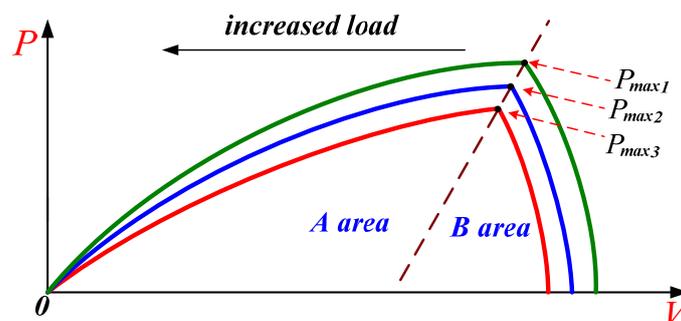


For a specific insolation, there exists one operating point where the PV array can generate its maximum output power. In order to achieve the best energy utilization of the PV arrays, an MPPT

algorithm with the perturbation-and-observation method must be integrated into the control strategy of the proposed power supply system. The perturbation-and-observation method has only required a few parameters to measure and control the maximum power point easily. Therefore, it is often applied to PV arrays energy for enhancing power capacity. Figure 9 shows the curves of output voltage *vs.* output power of PV arrays.

In Figure 9a, when the working point locates on point $A_1$, the load must be decreased to track the MPP of PV arrays. Similarly, when working point locates on $B_1$ in Figure 9b, the load must be increased to track the MPP of PV arrays. Therefore, the MPP of PV arrays can be obtained with a simple perturbation-and-observation method.

**Figure 9.** PV output power curves with respect to the PV output voltage: (**a**) operated in A area; (**b**) operated in B area.
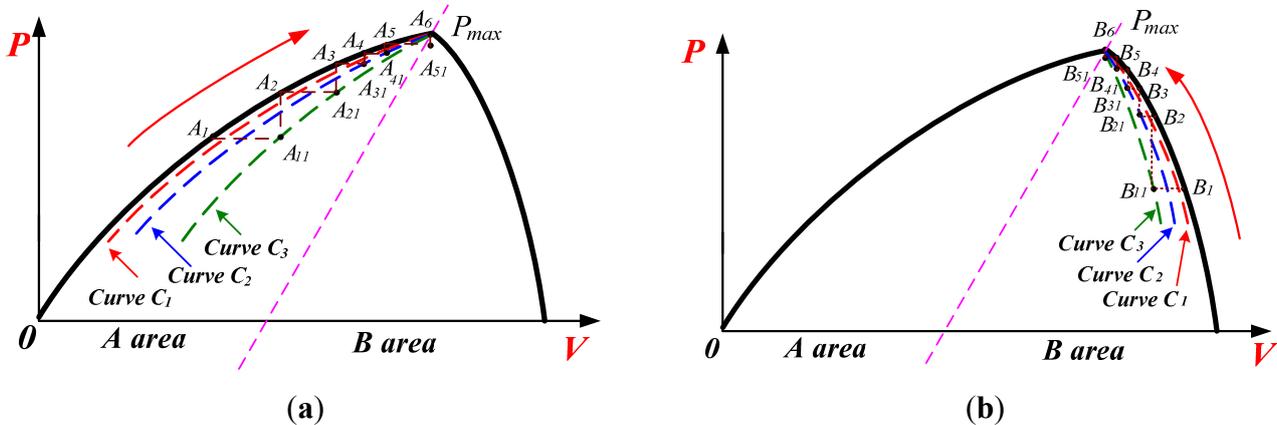


(**a**)          (**b**)

Figure 10 shows the emulator simulation system for the wind energy generator, in which the DC motor is controlled by different values of dc voltage $V_{DC,motor}$ to provide different limited maximum power for the load.

**Figure 10.** The emulator simulation system for the wind energy generator.
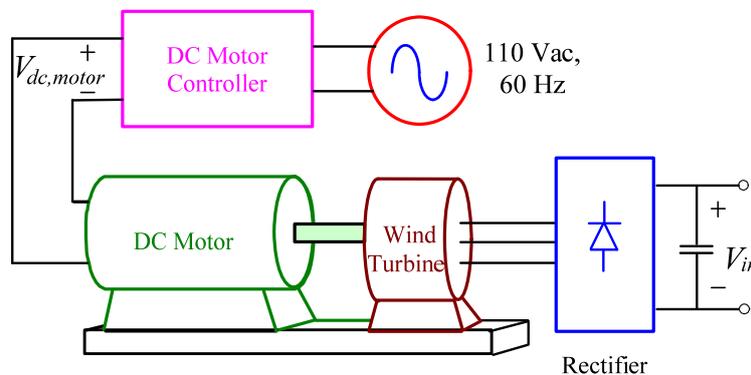


Figure 11 shows the typical output power characteristic curves of the wind turbine under different output voltages. The output power characteristic curves imply that the wind turbine will generate different maximum output powers for different wind speeds. Because the output power characteristic curves of the wind turbine are similar to those of the PV arrays shown in Figure 8, the perturbation-and-observation method is also adopted as the MPPT algorithm for the wind turbine.

**Figure 11.** Typical output power characteristic curves of the wind turbine under different wind speeds.
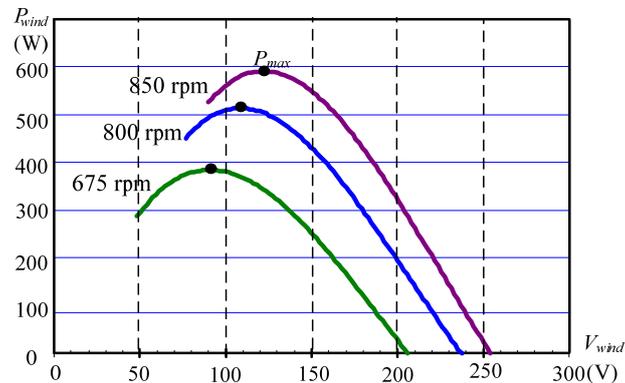


Figure 12 illustrates the flow chart of the MPPT algorithm of the PV arrays and wind turbine for the proposed power supply system. In the dual-input solar energy source and wind energy, the MPPT algorithm mentioned above is realized on a single-chip TMS320F240 microprocessor (Texas Instruments, Dallas, TX, USA).

**Figure 12.** Flow chart of perturbation-and-observation method for MPPT algorithm.
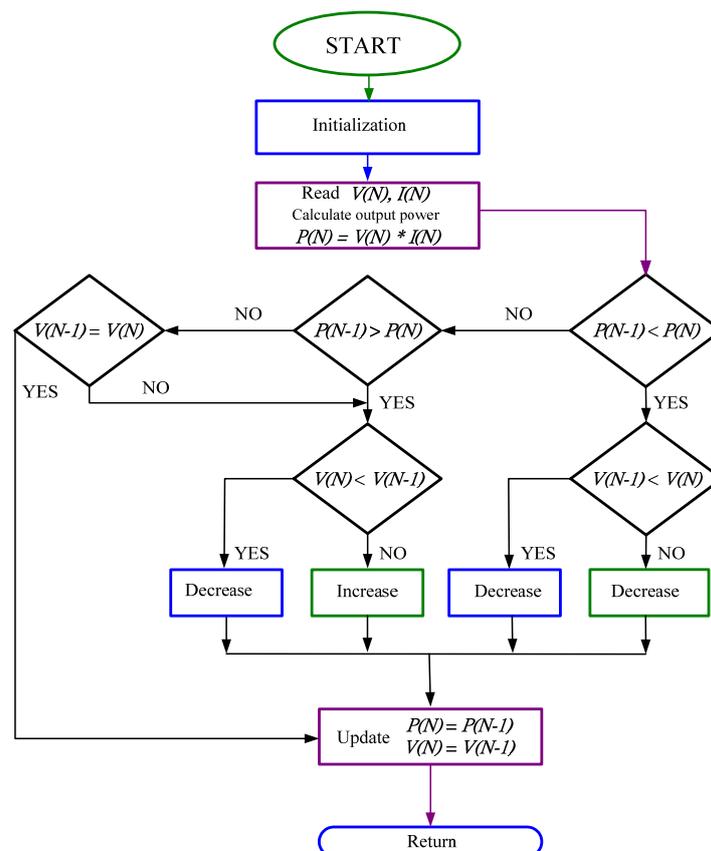


## 4. Control Scheme of the Proposed Power Supply

The conceptual control-block diagram of the proposed power supply system is shown in Figure 13. In practice, the control circuits are implemented with a TMS320F240 microcontroller for

drawing maximum power from the PV arrays and the wind turbine. The output voltage and current signals of the PV arrays and the wind turbine are sensed and transmitted to the microcontroller. The microcontroller will obtain the reference current signals *Iref1* and *Iref2* and generate two current error signals *ierror1* and *ierror2*. By comparing these error signals *ierror1* and *ierror2* to the sawtooth waveforms, the PWM comparator A and comparator B will generate desired gate driving signals *RelayA*(*signal*) and *RelayB*(*signal*) for the relays *A* and *B* to realize the MPPT control algorithm.

**Figure 13.** Conceptual control block diagram of the proposed power supply system.
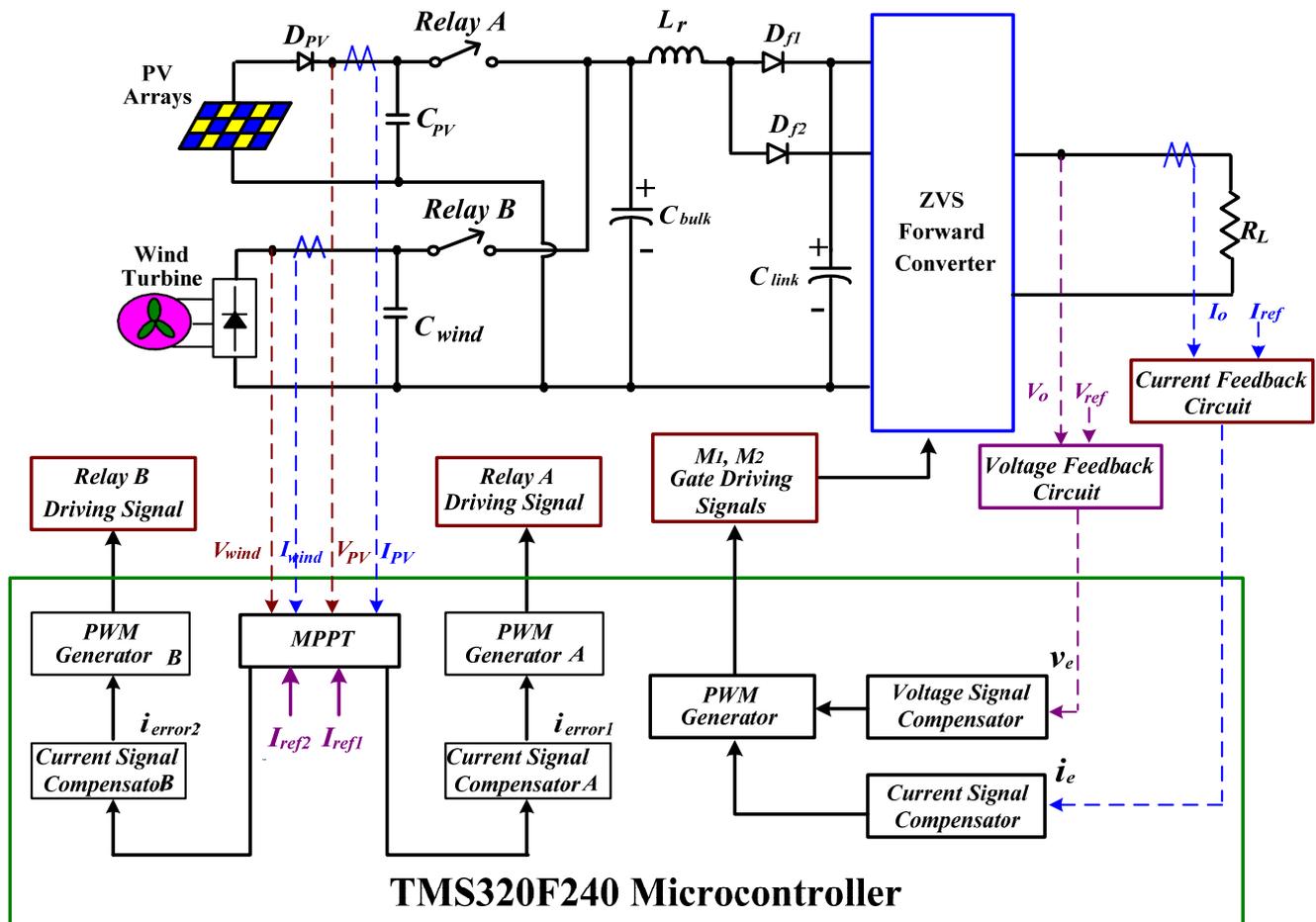


In order to regulate the output power, the voltage and current feedback compensators are essential. The voltage and current signals ($V_o$ and $I_o$) are obtained from the output terminal. By feedback compensators processing, the voltage error signal $v_e$ and current error signal $i_e$ will be obtained. Then, the PWM compensator will generate driving signals of switches ($M_1$ and $M_2$) to regulate the output power. To achieve an optimal stability and safety for the proposed small power system, functions of over-voltage protection, over-current protection and over-temperature protection are usually required. All of the protection signals are realized with the TMS320F240 microcontroller.

## 5. Design Consideration

To verify the feasibility, a 240 W prototype of the proposed power supply system was designed and built. Its key components are shown in Figure 3 and specifications are listed as follows:

(1)  PV arrays: peak power $P_{PV} = 300$ W, voltage $V_{PV} = 200\text{–}220$ V$_{DC}$,

(2)  Wind turbine: peak power $P_{wind} = 400$ W, voltage $V_{wind} = 200\text{–}230$ V$_{DC}$,

(3)  Output voltage of converter: $V_o = 24$ V$_{DC}$,

(4)  Output power of converter: $P_{o,max} = 240$ W, and

(5)  Switching frequency: $fs = 50$ kHz (*M1–M4*).

As followed are the design considerations and experimental results for the proposed dual-input power supply system.

## *5.1. Design Considerations of Key Components*

The key components of the proposed power supply system with a ZVS forward converter are considered as follows.

### 5.1.1. Design of isolation transformer ($T_r$)

In the proposed ZVS forward converter, the input voltage from minimum 200 V$_{DC}$ to maximum 230 V$_{DC}$ is considered. A maximum duty ratio $D_{max}$ corresponds to a minimum input voltage and a proper transformer turns ratio $n$. In order to obtain a proper transformer turns ratio $n$, we assume a maximum duty ratio as $D_{max} = 0.37$.

Once when maximum duty ratio $D_{max} = 0.37$ and minimum input voltage $V_{in(min)} = 200$ V$_{DC}$ are selected, the turn ratio of the transformer can be determined as:

$$n = \frac{D_{max} V_{in(min)}}{V_o} = \frac{(0.37)(200)}{24} = 3.08 \tag{3}$$

We take the turn ratio of the transformer $n = 3$. Thus, the maximum duty ratio $D_{max}$ will be revised as:

$$D_{max} = \frac{nV_o}{V_{in(min)}} = \frac{(3)(24)}{200} = 0.36 \tag{4}$$

A proper size of core ETD-39, ferrite material of TDK PC-40 and maximum flux $B_{max} = 0.2$ T (2000 G) are selected to minimize core losses. By applying the Faraday's law, primary turns $N_p$ of the transformer can be determined as:

$$N_p = \frac{DV_{in}}{A_c f_s \Delta B} = \frac{nV_o}{A_c f_s \Delta B} \tag{5}$$

where $A_c$ is the effective cross-section area of the transformer core ETD-39 with $A_c = 1.23$ cm$^2$, and $\Delta B$ is working flux density. For the forward converter, the transformer allows flux excursion in the first and the third quadrants of the B-H curve; that is:

$$\Delta B = 2B_{max} \tag{6}$$

with the flux density level $B_{max} = 0.2$ T, the transformer yields primary turns $N_p = 30$ and secondary turns $N_s = 10$.

### 5.1.2. Selection of Output Inductors ($L_1$ and $L_2$)

Inductor currents $i_{L1}$ and $i_{L2}$ are operated under continue conducting mode (CCM). Thus, the minimum inductor valve can be expressed as follows:

$$L_{1(min)} = L_{2(min)} = \frac{(1 - D_{max})}{2f_s}(\frac{V_o^2}{P_o})$$

$$= \frac{(1 - 0.36)}{2(50 \times 10^3)}(\frac{24^2}{240}) = 15.4\mu H \tag{7}$$

To assure the inductor current is operated at CCM, the inductor values of $L_1$ and $L_2$ are selected as 20 μH.

### 5.1.3. Selection of Synchronous Switches ($M_3$ and $M_4$)

The peak voltage stresses imposed on synchronous switches $M_3$ and $M_4$ can be determined as:

$$V_{DS3(max)} = V_{DS4(max)} = \frac{V_{in(max)}}{n} = \frac{230}{3} \approx 77V \tag{8}$$

The peak-to-peak variation in inductor current for $L_1$ or $L_2$ can be determined as:

$$\Delta i_L = \frac{V_o(1 - D_{max})}{2L_1 f_s}$$

$$= \frac{(24)(1 - 0.36)}{2(20 \times 10^{-6})(50 \times 10^3)} = 7.68A \tag{9}$$

and the maximum inductor current of $L_1$ and $L_2$ can also be determined as:

$$I_{L(max)} = \frac{I_o}{2} + \frac{1}{2}\Delta i_L = 5 + \frac{7.68}{2} = 8.84A \tag{10}$$

Therefore, the maximum current stresses of synchronous switches $M_3$ and $M_4$ can be determined as:

$$I_{DS3(max)} = I_{DS4(max)} = I_{L(max)} = 8.84A \tag{11}$$

Selection of power switches involves a trade-off between conduction losses and switching losses. MOSFETs with low $R_{ds(on)}$ can usually keep low conduction losses, but they usually have high parasitic capacitance and require a large die size. In this application, the active switch is IRFP244 with a drain-source breakdown voltage of 250 V, a drain current of 15 A, and a channel resistance of 0.28 Ω.

### 5.1.4. Selection of Main and Auxiliary Switch ($M_1$ and $M_2$)

For the ZVS forward converter, the peak voltage stresses imposed on main switch $M_1$ and auxiliary switch $M_2$ is:

$$V_{DS1(max)} = V_{DS2(max)}$$

$$= V_{in(min)}(\frac{1}{1 - D_{max}}) = 312.5V \tag{12}$$

When main switch $M_1$ is turned on, the maximum current $I_{DS1(max)}$ is expressed as:

$$I_{DS1(\max)} = (\frac{I_{L(\max)}}{n}) = 2.95\text{A}$$ (13)

When the auxiliary switch $M_2$ is turned on, the maximum current $I_{DS2(max)}$ is expressed as:

$$I_{DS2(\max)} = (\frac{I_{L(\max)}}{n})\sqrt{1-D_{\max}} = 2.36\text{A}$$ (14)

With a drain-source breakdown voltage of 500V, a drain current of 14 A and a low $R_{ds(on)}$ of 0.4 Ω, IRFP450 MOSFETs are used and applied to the active switches ($M_1$ and $M_2$).

5.1.5. Selection of Output Filter Capacitor ($C_o$)

The capacitance is selected according to the specification of voltage ripple level $\Delta V_o$, which is usually less than 1% of $V_o$. Hence, the filter capacitance can be determined as:

$$C_o = \frac{(1-D_{\max})}{8L_1(1\%)f_s^2} = 160\mu\text{F}$$ (15)

Thus, a capacitor with 200 μF/50 V is selected.

5.1.6. Selection of Resonant Inductor and Clamping Capacitor ($L_r$ and $C_c$)

In order to achieve ZVS at turn-on transition for the main switch $M_1$ and auxiliary switch $M_2$, there must be sufficient energy stored in resonant inductor $L_r$ to completely discharge the resonant capacitors $C_r$. It should be noted that the resonant capacitance $C_r$ is the lumped capacitance of junction capacitance ($C_{oss}$) of switch $M_1$ along with intra-winding capacitance ($C_{TR}$) of the isolation transformer. Thus, resonant capacitor $C_r$ can be approximated as:

$$C_r = \frac{4}{3}C_{oss} + C_{TR} = 0.83nF$$ (16)

where parasitic capacitance $C_{oss}$ of IRFP450 is about 400 pF and isolation-transformer capacitance $C_{Tr}$ is about 0.3 nF. The resonant capacitor is selected $C_r = 1$ nF. Therefore, the following inequality must be satisfied:

$$\frac{1}{2} \times L_r \times I_{DS1(\max)}^2 \geq \frac{1}{2} \times C_r \times V_{in(\max)}^2$$ (17)

the value of the resonant inductor can be determined as:

$$L_r \geq \frac{C_r \times V_{in(\max)}^2}{I_{DS1(\max)}^2} = 6.1\mu\text{H}$$ (18)

In general, a slightly larger $L_r$ may be selected to ensure ZVS condition. In this application, a resonant inductor $L_r = 12$ μH is selected.

The clamping capacitance of $C_c$ needs to be determined along with resonant inductor $L_r$. A large clamping capacitor will lead to a smaller clamping voltage ripple, but it will slow down the dynamic response to input voltage changes. An optimal design is to select clamping capacitance so that a half of

the resonant period is longer than the maximum off-time of switch $M_1$. Thus, the following relationship should hold:

$$2\pi\sqrt{L_r C_c} \gg (1 - D_{max})T_s \tag{19}$$

which yields:

$$C_c \gg \frac{(1 - D_{max})^2}{4\pi^2 f_s^2 L_r} \tag{20}$$

From Equation (20), the clamping capacitor of $C_c = 0.68$ μF/250 V is selected. According to above design consideration, the key component values of the proposed power supply system are shown in Figure 14.

**Figure 14.** Experimental circuit of the proposed dual-input power supply system.
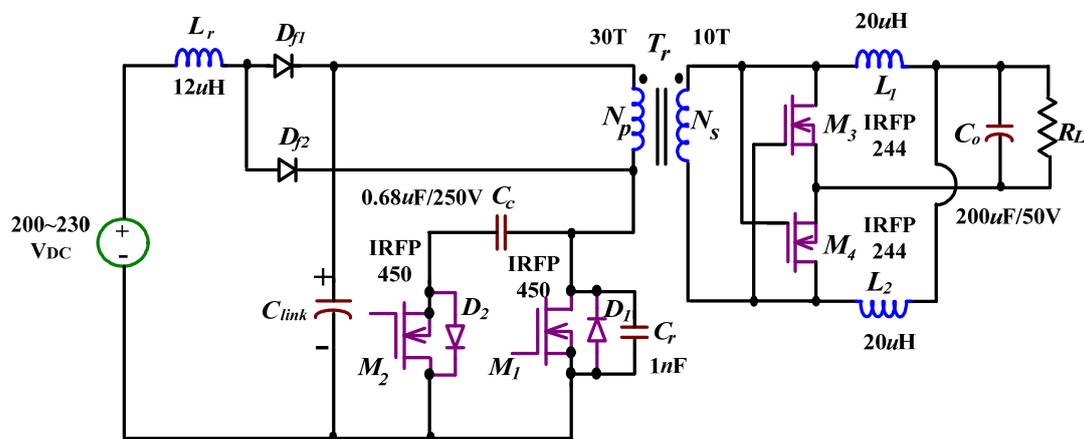


*5.2. Experimental Results*

The experimental results of key components for the proposed power supply system are described in this section. Figure 15 shows the measured date signal waveforms of power switches ($M_1$ and $M_2$). Figures 16 and 17 show measured voltage and current waveforms of active switches $M_1$ and $M_2$, from which it can be seen that the active switches $M_1$ and $M_2$ are operated under ZVS condition. Figure 18 shows the step-load change between 20% and 100% of the full load, from which it can be observed that the voltage regulation of output voltage $V_o$ has been limited within +1% to prove a good output dynamic response. Figure 19 shows measured output current, voltage and their corresponding power from start-up to the steady state for PV with perturbation-and-observation method. Figure 20 shows measured output current, voltage and power of PV arrays at variable MPPT algorithm. Figure 21 shows measured output current, voltage and their corresponding power from start-up to the steady state for wind turbine with perturbation-and-observation method. Figure 22 shows measured output current, voltage and power of wind turbine at variable MPPT algorithm. Figure 23 shows efficiency measurements of the proposed dual-input power supply system with ZVS forward converter, from which it can be seen that the maximum efficiency can reach as high as 91%.
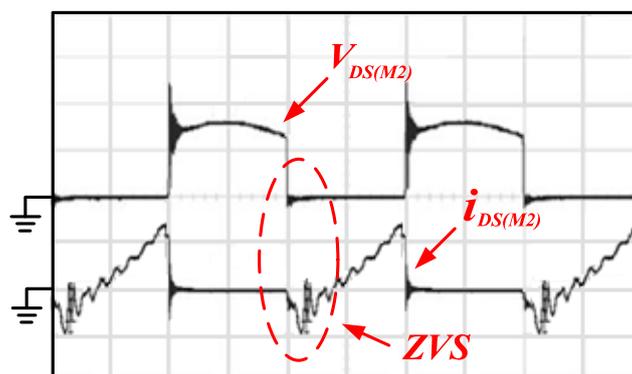
**Figure 15.** Measured gate signal waveforms of main switch $M_1$ and auxiliary switch $M_2$. ($V_{gs(M1)}$: 10 V/div; $V_{gs(M2)}$: 10 V/div; *time*: 5 μs/div).
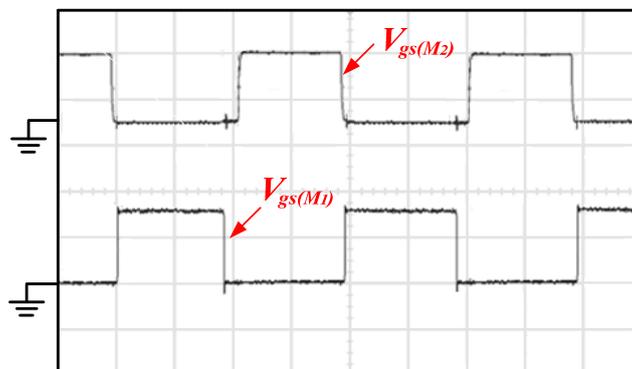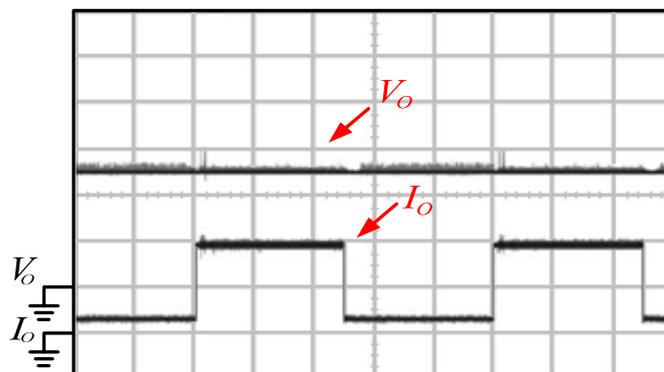


**Figure 16.** Measured voltage and current waveforms of switch $M_1$. ($V_{DS}$: 200 V/div; $i_{DS}$: 2 A/div; *time*: 5 s/div).
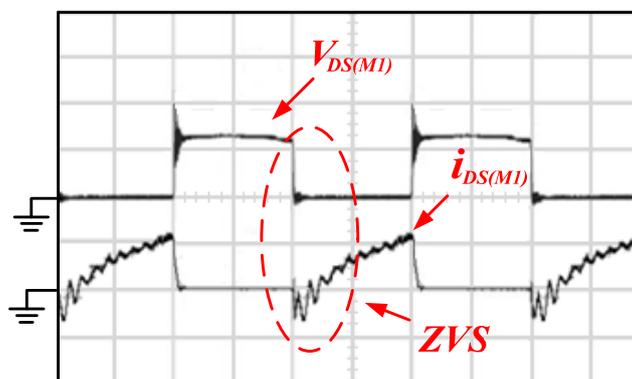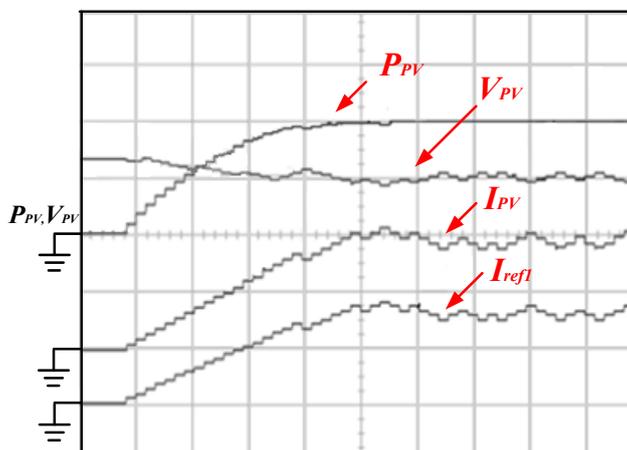


**Figure 17.** Measured voltage and current waveforms of switch $M_2$. ($V_{DS}$: 200 V/div; $i_{DS}$: 2 A/div; *time*: 5 μs/div).

**Figure 18.** Measured step-load changes between 20% and 100% of the full load. ($V_o$: 10 V/div; $I_o$: 5 A/div; *time*: 500 ms/div).
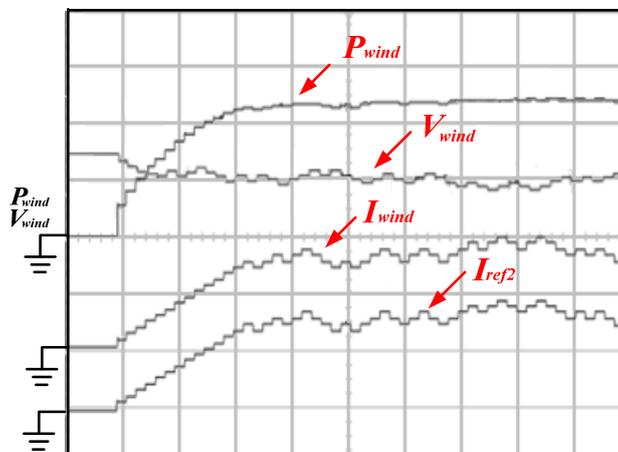


**Figure 19.** Measured output voltage, current and power waveforms of PV arrays at steady-state MPPT. ($P_{PV}$: 100 W/div, $V_{PV}$: 200 V/div, $I_{PV}$: 1 A/div, $I_{ref\_1}$: 1 V/div, *time*: 5 s/div).



**Figure 20.** Measured output voltage, current and power waveforms of PV arrays at variable MPPT. ($P_{PV}$: 100 W/div, $V_{PV}$: 200 V/div, $I_{PV}$: 2 A/div, $I_{ref\_1}$: 2 V/div, *time*: 10 s/div).
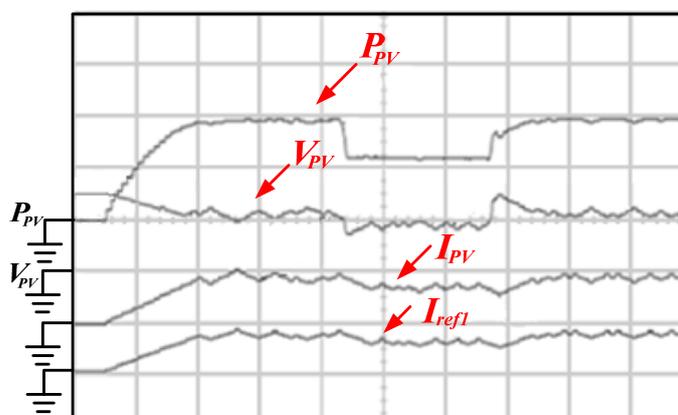
**Figure 21.** Measured output voltage, current and power waveforms of wind turbine at steady-state MPPT. ($P_{wind}$:100 W/div, $V_{wind}$:200 V/div, $I_{wind}$:1 A/div, $I_{ref\_2}$:1 V/div, *time*: 5 s/div).



**Figure 22.** Measured output voltage, current and power waveforms of wind turbine at variable MPPT. ($P_{wind}$: 100 W/div, $V_{wind}$: 200 V/div, $I_{wind}$: 2 A/div, $I_{ref2}$: 2 V/div, *time*: 10 s/div).
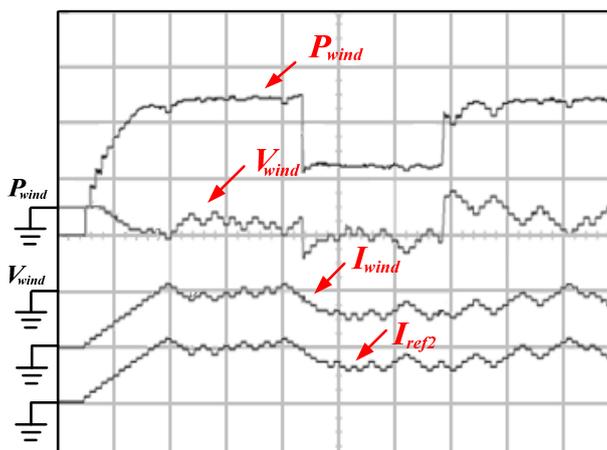


**Figure 23.** Plots of efficiency versus output current for the proposed dual-input power supply system with ZVS forward converter.
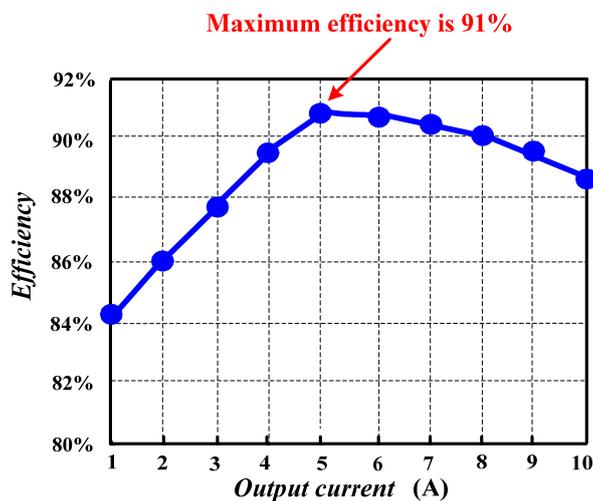
## 6. Conclusions

In this paper, a power supply system with a ZVS forward converter for renewable energy conversion is proposed. The proposed power supply system can alternatively draw power from PV arrays and wind turbines during weather or season changes. In order to obtain high conversion efficiency from the dual-input renewable energy, a forward converter with ZVS techniques is introduced. Both the MPPT algorithms of the PV arrays and the wind turbine are used with the perturbation-and-observation method to realize maximum power conversion. To achieve an optimally dynamic response and to increase control flexibility, a DSP and analog circuits are incorporated to implement MPPT algorithms and protect the system. Experimental results have verified that the proposed power supply system is relatively suitable for renewable energy source conversion.

## Conflicts of Interest

The authors declare no conflict of interest.

## References

1. Hepbasli, A. A comparative investigation of various greenhouse heating options using exergy analysis method. *Appl. Energy* **2011**, *88*, 4411–4423.
2. Bull, S.R. Renewable energy today and tomorrow. *IEEE Proc.* **2001**, *89*, 1216–1226.
3. Blusseau, P.; Patel, M.H. Gyroscopic effects on a large vertical axis wind turbine mounted on a floating structure. *Renew. Energy* **2012**, *46*, 31–42.
4. Sedaghat, A.; Mirhosseini, M. Aerodynamic design of a 300 kW horizontal axis wind turbine for province of Semnan. *Energy Convers. Manag.* **2012**, *63*, 87–94.
5. Hafez, O.; Bhattacharya, K. Optimal planning and design of a renewable energy based supply system for microgrids. *Renew. Energy* **2012**, *45*, 7–15.
6. Kuo, Y.-C.; Liang, T.-J.; Chen, J.-F. Novel maximum-power-point-tracking controller for photovoltaic energy conversion system. *IEEE Trans. Ind. Electron.* **2001**, *48*, 594–601.
7. Wakao, S.; Ando, R.; Minami, H.; Shinomiya, F.; Suzuki, A.; Yahagi, M.; Hirota, S.; Ohhashi, Y.; Ishii, A. Performance Analysis of the PV/Wind/Wave Hybrid Power Generation System. In Proceedings of the 3rd IEEE World Conference on Photovoltaic Energy Conversion, Osaka, Japan, 18 May 2003; Volume 3, pp. 2337–2340.
8. Chiu, H.-J.; Huang, H.-M.; Lin, L.-W.; Tseng, M.-H. A Multiple-Input DC/DC Converter for Renewable Energy Systems. In Proceedings of the IEEE International Conference on Industrial Technology, Hong Kong, China, 14–17 December 2005; pp. 1304–1308.
9. Matsuo, H.; Lin, W.Z.; Kurokawa, F.; Shigemizu, T.; Watanabe, N. Characteristics of the multiple-input DC–DC converter. *IEEE Trans. Ind. Electron.* **2004**, *51*, 625–631.
10. Cho, J.-G.; Baek, J.-W.; Jeong, C.-Y.; Yoo, D.-W.; Joe, K.-Y. Novel zero-voltage and zero-current-switching full bridge PWM converter using transformer auxiliary winding. *IEEE Trans. Power Electron.* **2000**, *15*, 250-257.
11. Chen, Y.-M.; Liu, Y.-C.; Hung, S.-C.; Cheng, C.-S. Multi-input inverter for grid-connected hybrid PV/wind power system. *IEEE Trans. Power Electron.* **2007**, *22*, 1070–1077.

12. Chen, Y.-M.; Liu, Y.-C.; Lin, S.-H. Double-input PWM DC/DC converter for high/low voltage sources. *IEEE Trans. Ind. Electron.* **2006**, *53*, 1538–1545.

13. Tseng, S.-Y.; Tsai, C.-T. Photovoltaic power system with an interleaving boost converter for battery charger applications. *Int. J. Photoenergy* **2012**, *2012*, doi:10.1155/2012/936843.

14. Tsai, C.-T.; Chen, S.-H. PV power-generation system with a phase-shift PWM technique for high step-up voltage applications. *Int. J. Photoenergy* **2012**, *2012*, doi:10.1155/2012/838231.

15. Shen, C.-L.; Tsai, C.-T. Double-linear approximation algorithm to achieve maximum-power-point tracking for PV arrays. *Energies* **2012**, *5*, 1982–1997.

16. Patel, H.; Agarwal, V. MPPT scheme for a PV-fed single-phase single-stage grid-connected inverter operating in CCM with only one current sensor. *IEEE Trans. Energy Convers.* **2009**, *24*, 256–263.

17. Tsai, C.-T. Energy storage system with voltage equalization strategy for wind energy conversion. *Energies* **2012**, *5*, 2331–2350.

18. Liu, K.-H.; Lee, F.C. Zero-voltage switching technique in DC/DC converter. *IEEE Trans. Power Electron.* **1990**, *5*, 293–304.

19. Tsai, C.-T.; Shen, C.-L. High step-down interleaved buck converter with active-clamp circuits for wind turbines. *Energies* **2012**, *5*, 5150–5170.